

Research Article

Effects of Temperature and Water on Mechanical Properties, Energy Dissipation, and Microstructure of Argillaceous Sandstone under Static and Dynamic Loads

Rongrong Zhang,^{1,2,3} Dongdong Ma ,^{1,2,3} Qingqing Su,^{1,2,3} and Kun Huang^{1,2,3}

¹State Key Laboratory of Mining Response and Disaster Prevention and Control in Deep Coal Mine, Anhui University of Science and Technology, Huainan, Anhui 232001, China

²School of Civil Engineering and Architecture, Anhui University of Science and Technology, Huainan, Anhui 232001, China

³Research Center of Mine Underground Engineering, Ministry of Education, Anhui University of Science and Technology, Huainan, Anhui 232001, China

Correspondence should be addressed to Dongdong Ma; dongdonm@126.com

Received 27 May 2020; Revised 17 June 2020; Accepted 19 June 2020; Published 20 July 2020

Academic Editor: Xianjie Hao

Copyright © 2020 Rongrong Zhang et al. This is an open access article distributed under the Creative Commons Attribution License, which permits unrestricted use, distribution, and reproduction in any medium, provided the original work is properly cited.

RMT-150B rock mechanics and split Hopkinson pressure bar (SHPB) devices were adopted to investigate the physical and mechanical properties, energy dissipation, and failure modes of argillaceous sandstone after different high temperatures under air-dried and saturation states. In addition, SEM and EDS tests were conducted to investigate its microstructure characteristics. Results showed that both the P-wave velocity and density of argillaceous sandstone specimen decreased with the increase of high temperature, while its porosity increased. Compared with static stress-strain curves, there was no obvious compaction stage for dynamic stress-strain curves, and the decrease rate of dynamic curves after peak strain was obviously slow compared with static curves. Both the static and dynamic strengths of argillaceous sandstone specimens decreased with increasing temperature, and the critical temperature point for the strength of argillaceous sandstone was 400°C. At the same temperature, the specific energy absorption under air-dried state was generally smaller compared with that under saturated state. Both the strain rate and temperature showed significant effect on the failure mode. After 100~1000°C heat treatment, the granular crystals of the clastic structure gradually became larger, and both the number and average size of the original pores decreased, resulting in the deterioration of mechanical properties of argillaceous sandstone specimen.

1. Introduction

The mining of deep mineral resources would inevitably encounter the problem that the ground temperature increased gradually with the increase of depth, and engineering geological monitoring results showed that the average temperature gradient range was 30~200°C/km [1–3]. The temperature of underground rock engineering, such as nuclear waste storage, could reach about 300°C caused by nuclear decay [4–6]. Moreover, in the process of coal vaporization, the surrounding rock temperature would eventually reach 1000°C [7–9]. Research results revealed that

the deep surrounding rock bared coupled high temperature, water content, and dynamic stress derived from the impact of blasting and machinery. Therefore, considering the effects of high temperature, water, and external dynamic force on rock was necessary for solving deep rock problems.

Obvious dynamic response characteristics were found for deep rock mass suffering from mechanical disturbance, explosion, and other impact loads, and there was obvious difference under static load [10–12]. Theoretically, strain rate was the standard for dividing the loading type (e.g., creep, static, and dynamic) of rock, as shown in Figure 1. Numerous theories and laboratory test results indicated that

split Hopkinson pressure bar (SHPB) device could accurately test the high strain rate response of materials within strain rate ranges of $10^2\sim 10^3\text{ s}^{-1}$ [13].

Previous studies on the thermal damage of rock materials mainly focused on the effect of temperature on its static and dynamic mechanical properties [14–16], and the test results showed that both the P-wave velocity and density of rock decreased with the increase in temperature [17–19]. In addition, the static peak stress and elastic modulus decreased gradually with increasing temperature [20–22]. Ding et al. [23] performed the uniaxial and triaxial compression experiments on sandstone from 20°C to 800°C and indicated that tensile and shear fractures formed during unloading at the lower initial confining pressure, while sliding of the microcracks occurred during unloading at the higher initial confining pressure. Meng et al. [24] studied the influence of temperature on the physical and microstructure of limestone. Test results showed that limestone pore fractal dimension decreased gradually with increasing temperature. Moreover, the temperature threshold interval (400°C to 500°C) was observed based on the pore structure change. Liu and Xu [25, 26] analyzed the relationships among peak stress, peak strain, and elastic modulus of marble and high temperature. Yin et al. [27] investigated the stress-strain curve characteristic, elastic modulus, dynamic damage, and energy dissipation of rock with various high temperatures. Li et al. [28] found that, above 600°C, the granite specimens generated a large number of obvious large cracks and volume expansion, and their thermal conductivity decreased rapidly. In addition, scanning electron microscopy (SEM) and X-ray diffraction (XRD) techniques illustrated that high temperature would lead to the phase transition of quartz inside rock, resulting in obvious changes in physical and mechanical properties of rock materials [29–31]. Water was a crucial factor affecting physical and mechanical properties of rock materials. Hence, it was essential to establish the water sensitivity of rock to the deformation and strength in rock engineering. For instance, Wang et al. [32] studied the effects of water content and confining pressure on the physical and mechanical properties and energy evolution characteristics of rocks under uniaxial and triaxial states. Results showed that the critical elastic energy decreased linearly as the water content increased. In addition, experimental studies for dry and water-saturated rock materials were carried out to explain the variation in strength and elasticity modulus with water content [33, 34].

All the mentioned results were obtained by considering the effect of water or temperature, while limited studies focused on the physical and mechanical properties of rock with various water contents after high temperature treatment. In this paper, argillaceous sandstone collected from –725 m depth of a coalmine was selected, and attempts were made to explore the water saturation effects on the static and dynamic mechanical properties, energy dissipation characteristics, and failure mode of argillaceous sandstone after different high temperatures. Scanning electron microscopy (SEM) and energy dispersive spectrometer (EDS) tests were conducted to investigate the microscopic morphological and damage characteristics of rocks after high temperature

treatment under air-dried and saturated states. Study results could provide scientific basis for rapid excavation and safety stability analysis of deep rock engineering.

2. Specimen Preparation and Experiment Device

2.1. Sample Preparation. The argillaceous sandstone used in this study was collected from –735 m depth of Xieqiao coalmine in Huainan city, Anhui province, China. The average P-wave velocity and average porosity of argillaceous sandstone were 2778 m/s and 1.47%, respectively. The main components of argillaceous sandstone were quartz which accounted for 48.5%, 24.0% albite, 10.1% kaolinite, 2.7% calcite, and other minerals, as shown in Figure 2(a). The integrity of the microstructures of the samples was good under natural conditions, as shown in Figure 2(b). Sample processing dimensions and methods complied with ISRM [35] (International Society for Rock Mechanics) standard. The diameter of rock specimen was 50 mm, while its length was 100 mm and 25 mm for static and dynamic tests, respectively.

2.2. Hydrothermal Treatment and Testing Device. In this test, 7 temperature gradients were arranged for heating argillaceous sandstone specimens: 20°C (room temperature), 100°C, 200°C, 400°C, 600°C, 800°C, and 1000°C. SX-5-12 box-type resistance furnace with maximum temperature of 1200°C was used to heat specimens, and the heated rate was 6°C/min. It would be maintained for 4 hours after reaching the desired temperature and then cooled to room temperature naturally in the resistance furnace. Finally, the thermal treated rock specimens were divided into two groups (saturated and air-dried states), and the air drying and water filling treatment were carried out by drying box and vacuum water filling machine for 48 h, respectively. After high temperature and water treatment, argillaceous sandstone specimens were prepared for conducting static and dynamic tests, SEM test, and EDS test. The experiment device and procedures are shown in Figure 3. In SHPB tests, the dynamic strain, stress, and strain rate could be obtained using the “three-wave” method [36, 37].

3. Test Results and Analysis

3.1. Variation in P-Wave Velocity, Dry Density, and Porosity. The P-wave velocity, density, and porosity were important parameters to reflect the damage degree of rock materials. The variations in P-wave velocity, density, and porosity of argillaceous sandstone samples with temperature were obtained and shown in Figure 4. With increasing temperature, both the P-wave velocity and density of argillaceous sandstone gradually decreased, while the porosity showed an opposite trend. Moreover, the variation of these three parameters was small when the temperature increased from 20°C to 200°C. For instance, the average P-wave velocity of argillaceous sandstone decreased from 2777.91 m/s (20°C) to 2642.72 m/s (200°C), with the reduction rate of 4.87%. After

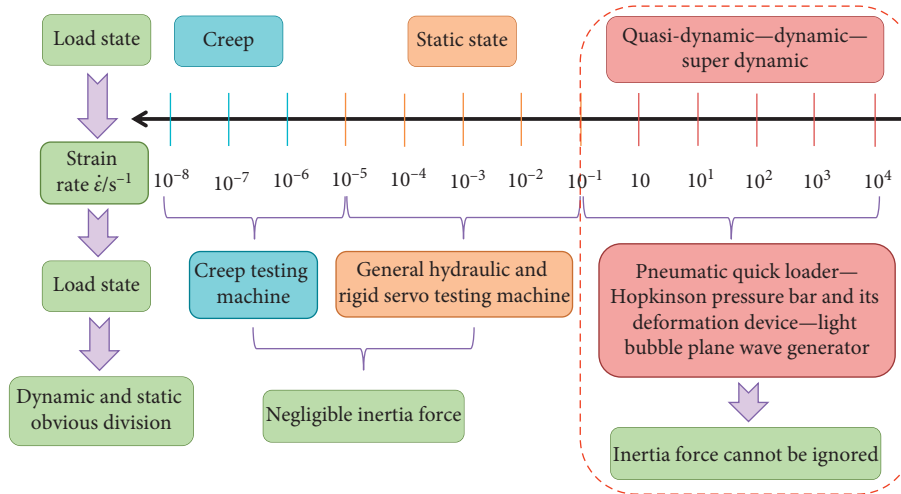


FIGURE 1: Loading type classified by strain rate.

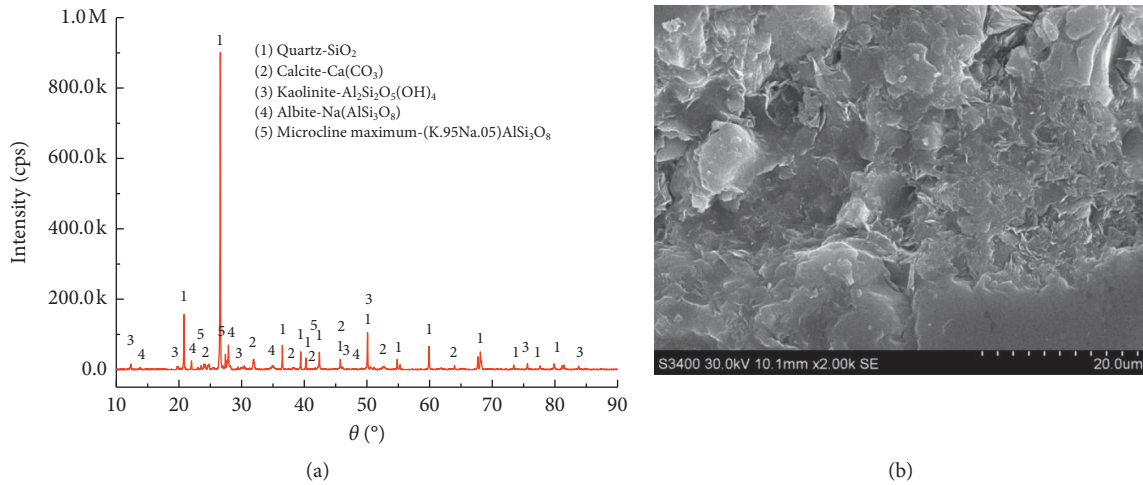


FIGURE 2: XRD spectrum and SEM observation of argillaceous sandstone sample (20°C). (a) XRD results. (b) SEM results.



FIGURE 3: Experiment device and test procedures.

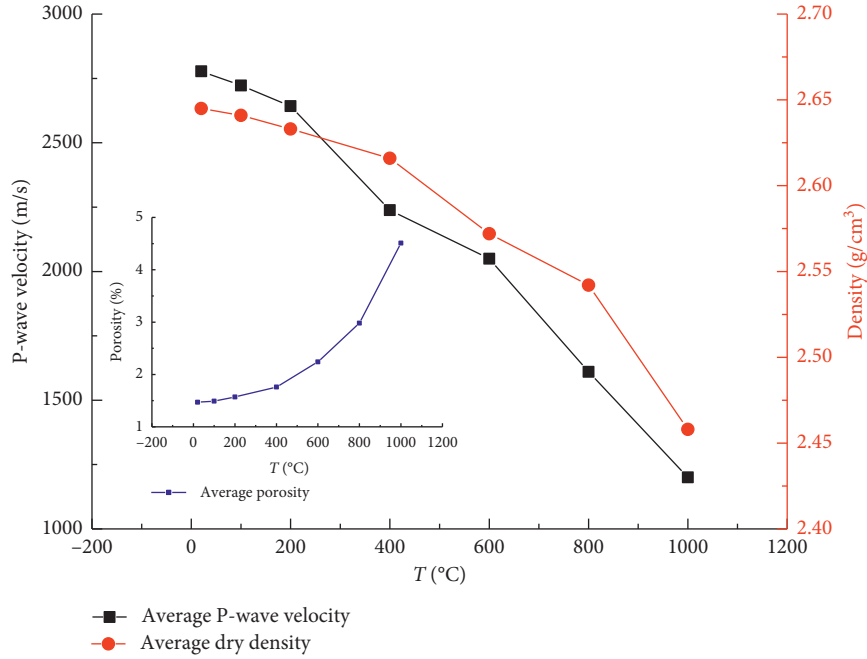


FIGURE 4: Variation in P-wave velocity, dry density, and porosity with high temperature.

400°C, the variation rates of P-wave velocity, density, and porosity were significantly faster, and the average porosity of argillaceous sandstone was 4.51% at 1000°C, which was 2.58 times higher than that at 400°C.

3.2. Static and Dynamic Stress-Strain Curves. The static and dynamic stress-strain curves of argillaceous sandstone with two water contents after different high temperatures are shown in Figures 5 and 6, respectively. In this research, the meanings of letters in the graphs and tables were as follows: the first letter represented the load type (static or dynamic), the second letter represented the water content state (air-dried or saturated), and the number represented the temperature value. For instance, “S-S-600” represented argillaceous sandstone under saturated state after 600°C temperature in static uniaxial compression test. It can be seen from Figures 5 and 6 that similar change trends were found for static stress-strain curves of argillaceous sandstone under the air-dried and saturated state, which could be divided into four stages: compaction stage, linear elastic stage, plastic deformation stage, and failure stage. With the increase of temperature, the peak stress of argillaceous sandstone decreased, while the peak strain increased. Compared with static stress-strain curves, there was no obvious compaction stage for dynamic stress-strain curves, and the decrease rate of dynamic curves after peak strain was obviously slow compared with static curves.

3.3. Static and Dynamic Compressive Strength. Static and dynamic strengths of argillaceous sandstone under different test conditions are presented in Figure 7. In addition, to describe the effect of water on strength of argillaceous sandstone, the relative peak stress (K) was defined and could be calculated:

$$K = \frac{\sigma_S - \sigma_A}{\sigma_S}, \quad (1)$$

where σ_S and σ_A were the strengths of argillaceous sandstone specimen under the saturated state and air-dried state, respectively.

Figure 7 illustrated that both the static and dynamic strengths of argillaceous sandstone specimens decreased with increasing temperature. Moreover, the decrease speed from 400°C to 600°C was obviously slower compared with other temperature scopes under different test conditions. The mechanism behind this phenomenon could be explained as follows: rock materials were composed of different mineral particles; the thermal expansion coefficients of various mineral particles of rocks were different under high temperature. Hence, small deformation and thermal stress were generated during heating process, resulting in the damage of argillaceous sandstone specimen. In addition, the quartz α - β phase had an irreversible change at 573°C [29], as shown in Figure 8. Two Si-O tetrahedrons in the crystal structure changed from the angle of 150° to 180°, which was of benefit to soften property of rock specimen. Moreover, OH⁻ and H⁺ would be separated from the mineral skeleton at 450~500°C, and the loss of component water and crystal water would lead to further destruction of mineral crystal structure [38].

It could be found that, after the same temperature, the static compressive strength of argillaceous sandstone at saturated state was small compared with that at air-dried state. However, its dynamic compressive strength at saturated state was higher than that at air-dried state. Additionally, from the variation in K with temperature it could be noticed that the value of dynamic relative peak stress was between 0.12 and 0.35, and it increased with the increase of temperature. Under static load, the loading speed was lower than that of crack propagation; hence, the

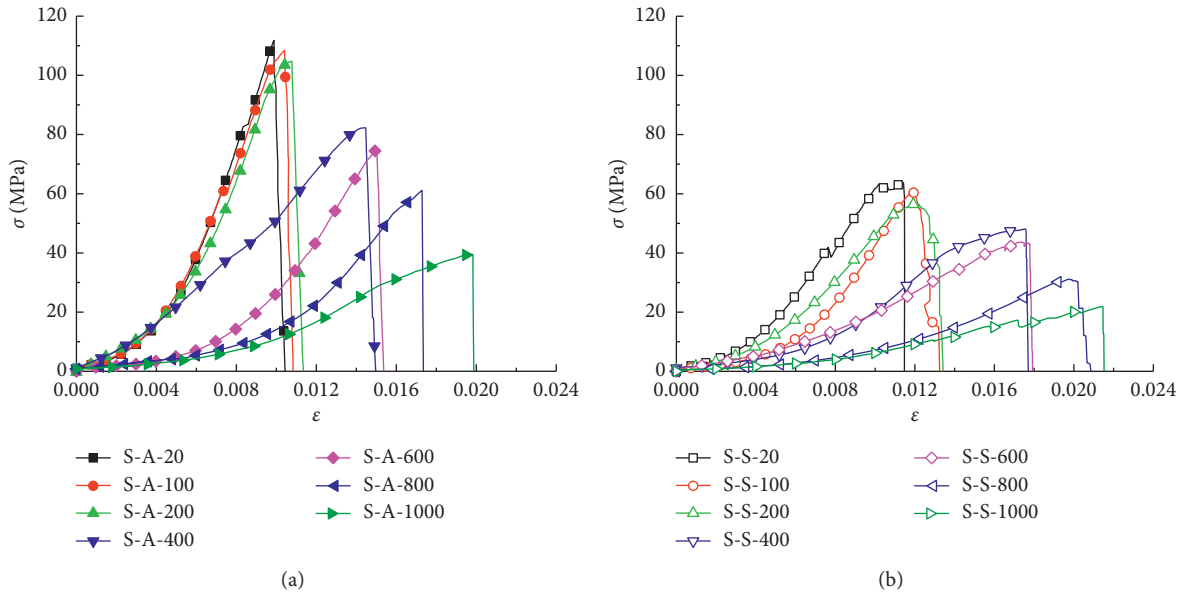


FIGURE 5: Static uniaxial compression stress-strain curves of argillaceous sandstone after high temperature. (a) Air-dried state. (b) Saturation state.

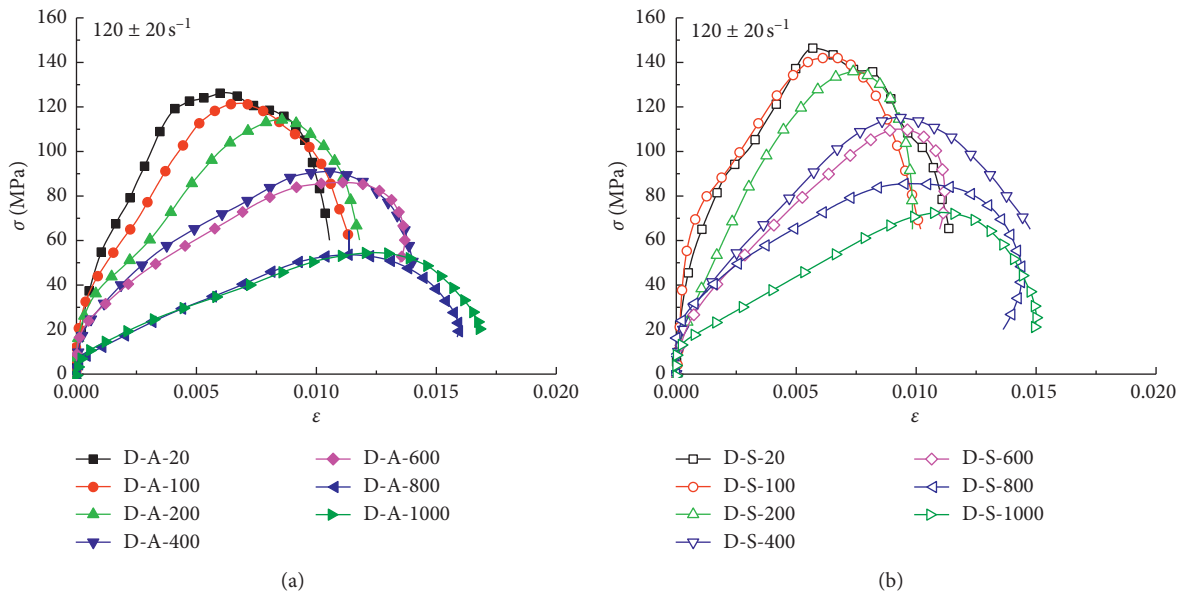


FIGURE 6: Continued.

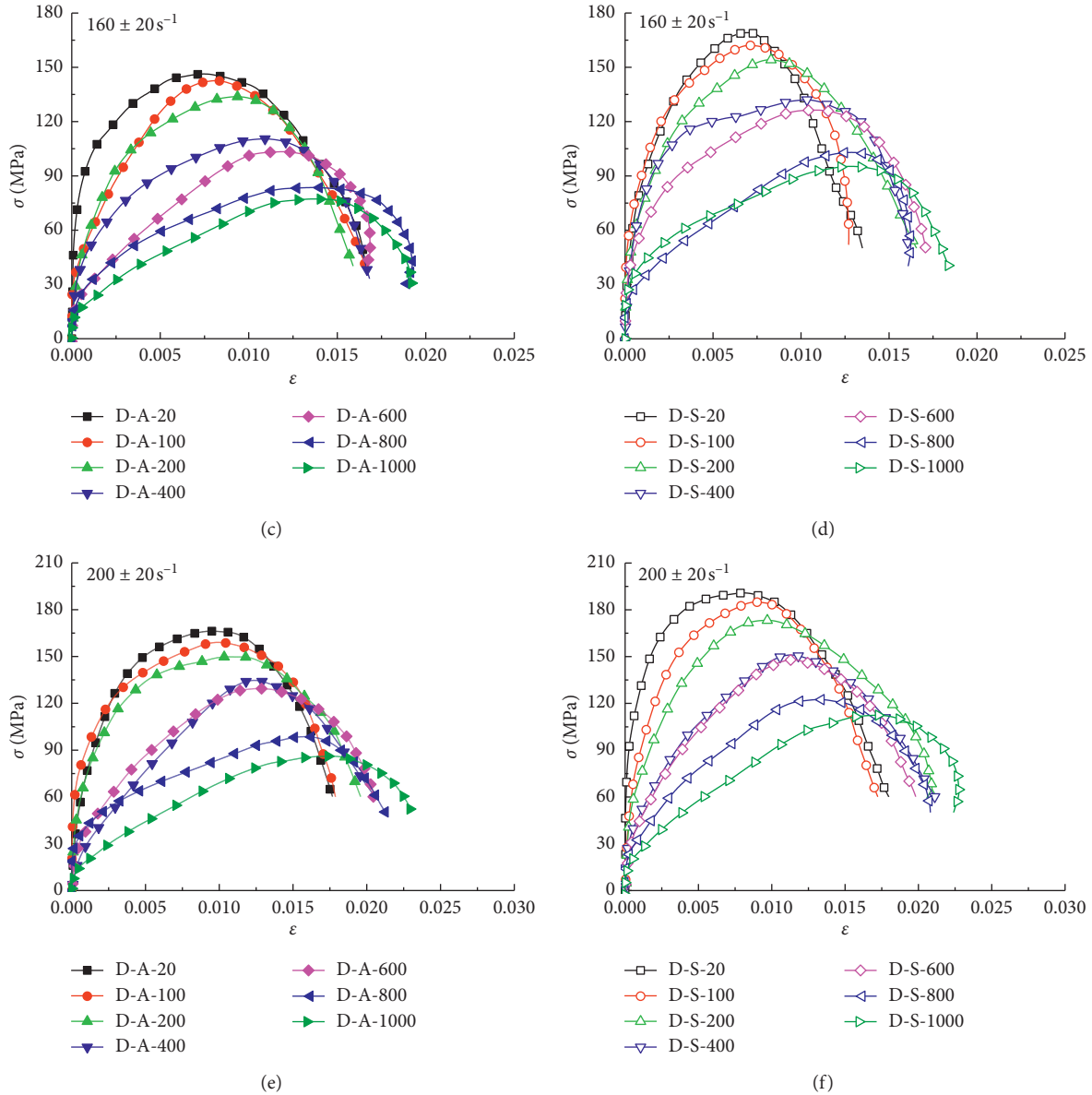


FIGURE 6: Dynamic uniaxial compression stress-strain curves of argillaceous sandstone after high temperature. (a) Air-dried state ($120 \pm 20s^{-1}$). (b) Saturation state ($120 \pm 20s^{-1}$). (c) Air-dried state ($160 \pm 20s^{-1}$). (d) Saturation state ($160 \pm 20s^{-1}$). (e) Air-dried state ($200 \pm 20s^{-1}$). (f) Saturation state ($200 \pm 20s^{-1}$).

saturated flowing water in the rock would have sufficient time to diffuse to the newly expanded crack. At the same time, the expansion of free water in the crack would produce a similar “siphon” effect and reach the crack tip, which played a role in lubricating the crack contact surface and promoted the crack growth [21]. However, under dynamic load, the crack propagation speed was much faster than that under static load, and free water had no enough time to expand into the crack during failure process. At this time, the water played a cohesive strength to prevent the crack growth on the fracture surface; moreover, Stefan effect caused by free water in the crack surface of water bearing sandstone would produce a reaction force to prevent the separation of the two crack surfaces [39], leading to higher strength of water-saturated rock under dynamic load.

It could be found that strain rate effect was observed for argillaceous sandstone with two water states. To quantitatively describe the increment of strength behavior of argillaceous sandstone after high temperature treatment caused by strain rate, the dynamic compressive strength increase factor under air-dried state (DCFA) and saturated state (DCFS) was defined, which could be calculated:

$$DCFA = \frac{\sigma_{D,A,T}}{\sigma_{S,A,T}}, \quad (2)$$

$$DCFS = \frac{\sigma_{D,S,T}}{\sigma_{S,S,T}}, \quad (3)$$

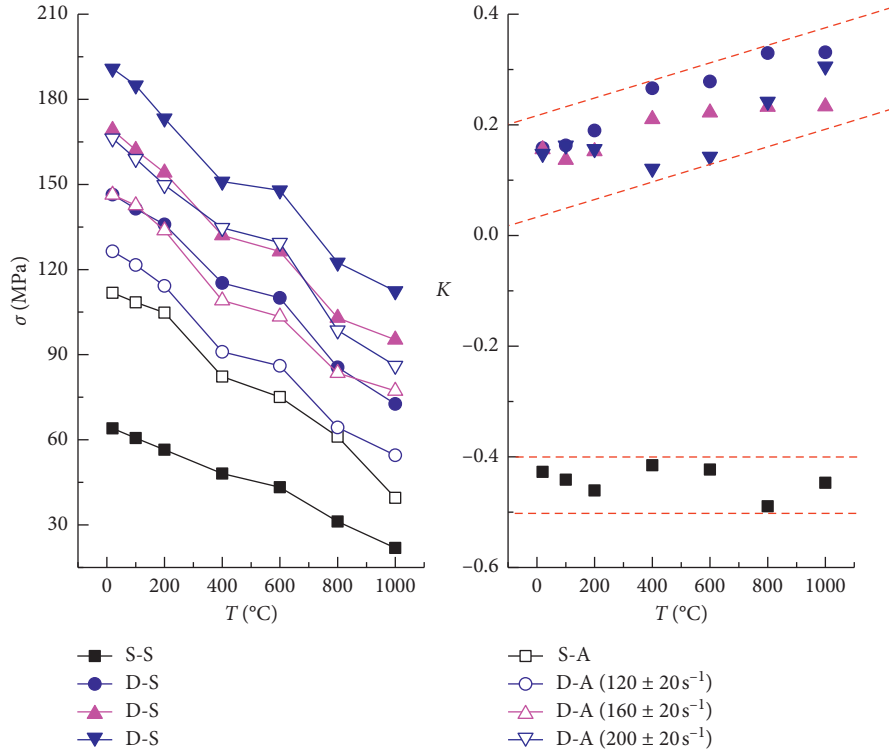


FIGURE 7: Static and dynamic strengths of argillaceous sandstone under different test conditions.

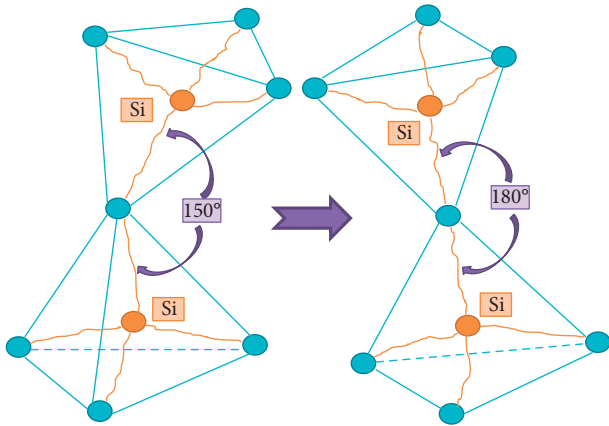


FIGURE 8: Sketches of the α - β quartz bond angle.

where $\sigma_{D,A,T}$ and $\sigma_{S,A,T}$ were the dynamic and static strengths of argillaceous sandstone specimen after high temperature treatment under the air-dried state, respectively; $\sigma_{D,S,T}$ and $\sigma_{S,S,T}$ were the dynamic and static strengths of argillaceous sandstone specimen after high temperature treatment under saturated state, respectively.

Figure 9 displays variation in DCFA and DCFS of argillaceous sandstone with temperature. It could be seen that the values of both DCFA and DCFS were larger than 1, showing obvious strain rate strengthening effect. Under the same high temperature and strain rate, the value of DCFS was much higher than that of DCFA; for instance, the dynamic growth factor with saturated state at 600°C under

$120 \pm 20 \text{ s}^{-1}$ was 2.54, which was higher than the value of 1.15 with air-dried state. This phenomenon demonstrated that water was of benefit to increase the strength growth rate of argillaceous sandstone under dynamic load. Under the same water content state, DCFS increased with the increase of strain rate and temperature; moreover, its increment was obvious after 400°C .

3.4. Variation in Energy Dissipation and Mass Fractal Dimension. Previous investigation demonstrated that specific energy absorption could reflect the energy dissipation ability of rock under dynamic load [40], which could be obtained by the following equation:

$$\xi = \frac{W_S}{V}, \quad (4)$$

where W_S was the absorption energy of argillaceous sandstone specimen; V was the volume of argillaceous sandstone specimen.

In addition, to further illuminate the fracture characteristic of argillaceous sandstone after different high temperatures, the fracture result was quantified by mass fractal dimension of fragmentation. The rock fragments were collected and screened by different sizes after SHPB test. The sizes were 0.15 mm, 0.3 mm, 0.6 mm, 1.18 mm, 2.36 mm, 4.75 mm, 9.5 mm, 13.2 mm, 16 mm, 19 mm, 26.5 mm, 31.5 mm, and 37.5 mm, and the typical grading curve is displayed in Figure 10.

After obtaining the mass fractal dimension of fragmentation under different test conditions, the fragment distribution parameters could be calculated:

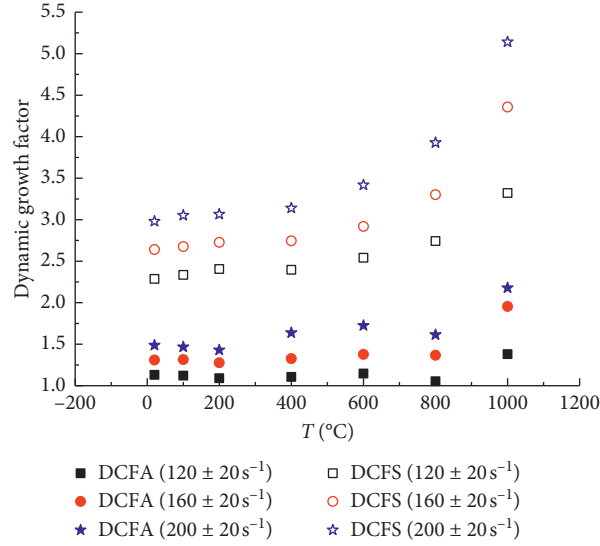


FIGURE 9: Relationship between dynamic increase factor and temperature.

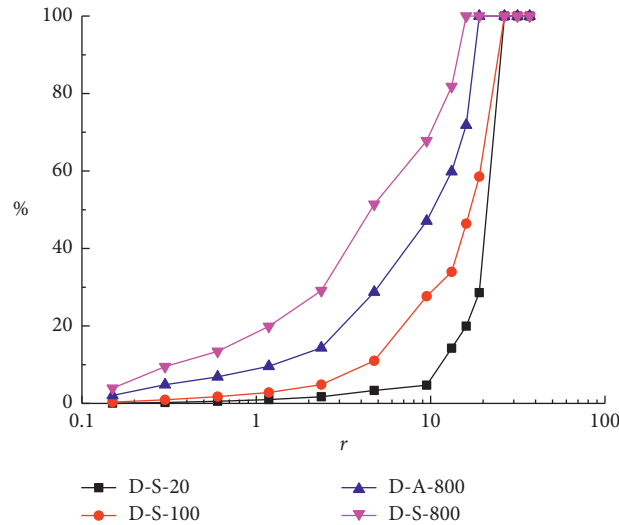


FIGURE 10: Typical grading curve of argillaceous sandstone specimen.

$$\frac{m_r}{M} = \left(\frac{r}{r_m} \right)^b, \quad (5)$$

$$b = \frac{\ln(m_r/M)}{\ln r}, \quad (6)$$

$$D = 3 - b, \quad (7)$$

where m_r was accumulative mass under sieve of characteristic size r ; M was total mass of specimen; r_m was particle size; b was fragment distribution parameter; D was the mass fractal dimension of fragmentation.

Figure 11 displays the specific energy absorption and mass fractal dimension of fragmentation of argillaceous sandstone with various temperatures and water content states. At the same temperature, the specific energy

absorption increased with increasing strain rate after high temperature for two water content states. In addition, the specific energy absorption under air-dried state was generally smaller compared with that under saturated state.

The relationship among mass fractal dimension, specific energy absorption of argillaceous sandstone, and strain rate is shown in Figure 12. With the increase of strain rate, both the specific energy absorption and mass fractal dimension increased continuously after the same temperature. Moreover, the specific energy absorption and the mass fractal dimensions showed positive correlation. The value of specific energy absorption reflected the energy consumed per unit volume of rock specimen; hence, larger specific energy absorption led to more deformation and damage of rock specimen, resulting in more fracture surfaces and smaller scale fragments.

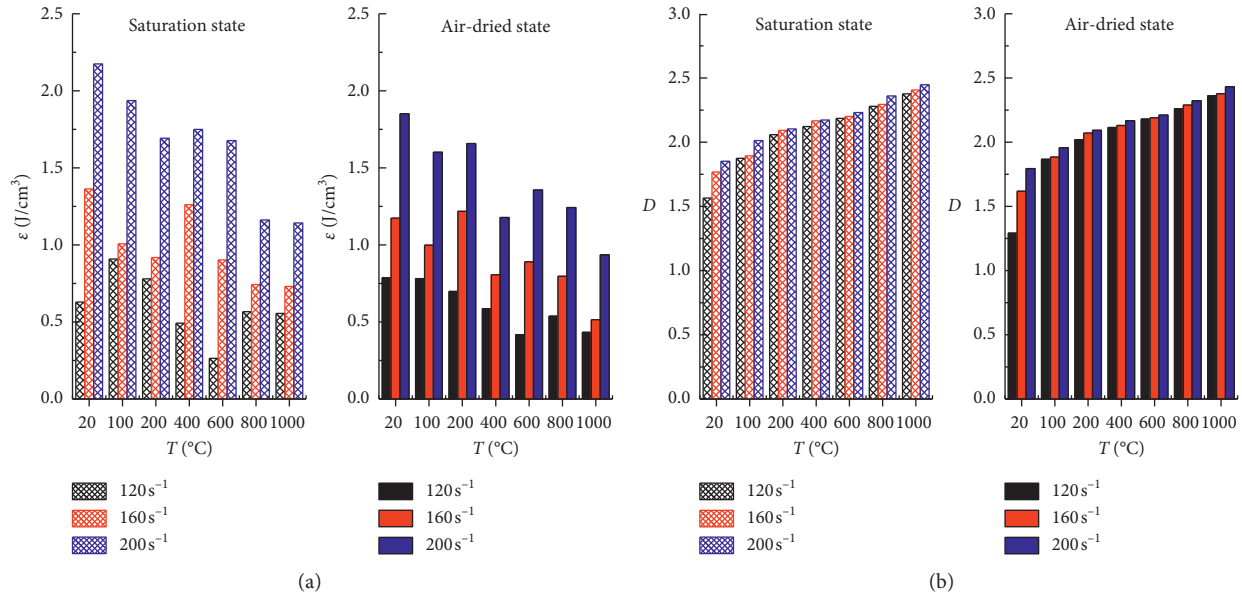


FIGURE 11: The specific energy absorption and mass fractal dimension of fragmentation of *argillaceous sandstone* with various temperatures and water content states. (a) Specific energy absorption values. (b) Mass fractal dimension.

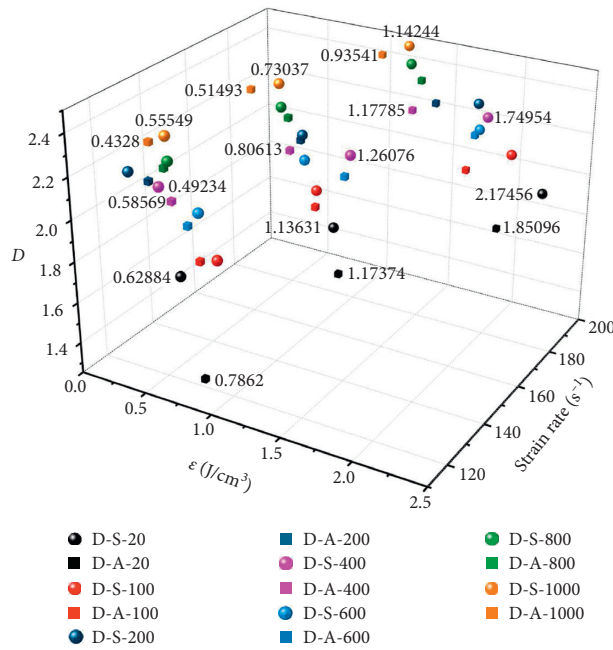


FIGURE 12: The relationship among mass fractal dimension, specific energy absorption, and strain rate.

3.5. *Static and Dynamic Failure Modes of Argillaceous Sandstone.* Figure 13 shows the typical static failure modes of argillaceous sandstone specimen with air-dried state after different high temperatures. It could be noticed that, after 20°C, 100°C, and 200°C, cracks paralleled to the axial direction and diagonal connection were observed for argillaceous sandstone specimen, and the corresponding failure modes were mainly shear and splitting, as shown in Figures 13(a), 13(b), and 13(c). As a contrast, after 400°C, 600°C, and 800°C, the argillaceous sandstone specimen presented coupled shear and splitting failure; in addition,

partial compression failure was observed, caused by high temperature damage, as shown in Figures 13(d), 13(e), and 13(f). After 1000°C, large damage for internal structure was generated inside argillaceous sandstone specimen, and it was almost without bearing capacity; hence, collapse appeared under external load, as shown in Figure 13(g).

The dynamic impact compression failure modes of argillaceous sandstone under air-dried state with various strain rates and high temperatures are shown in Figure 14. Both the strain rate and temperature showed significant effect on the failure mode. At $120 \pm 20 \text{ s}^{-1}$, tensile cracks were observed

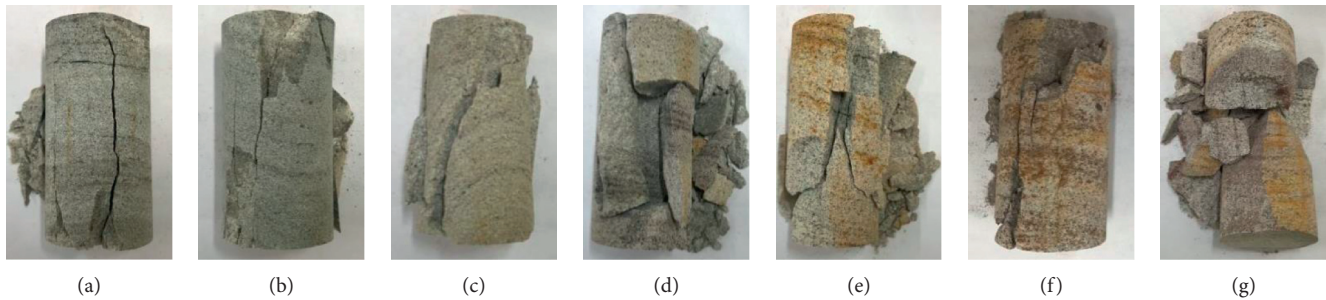


FIGURE 13: Static failure mode of argillaceous sandstone after high temperature. (a) 20°C. (b) 100°C. (c) 200°C. (d) 400°C. (e) 600°C (f) 800°C. (g) 1000°C.

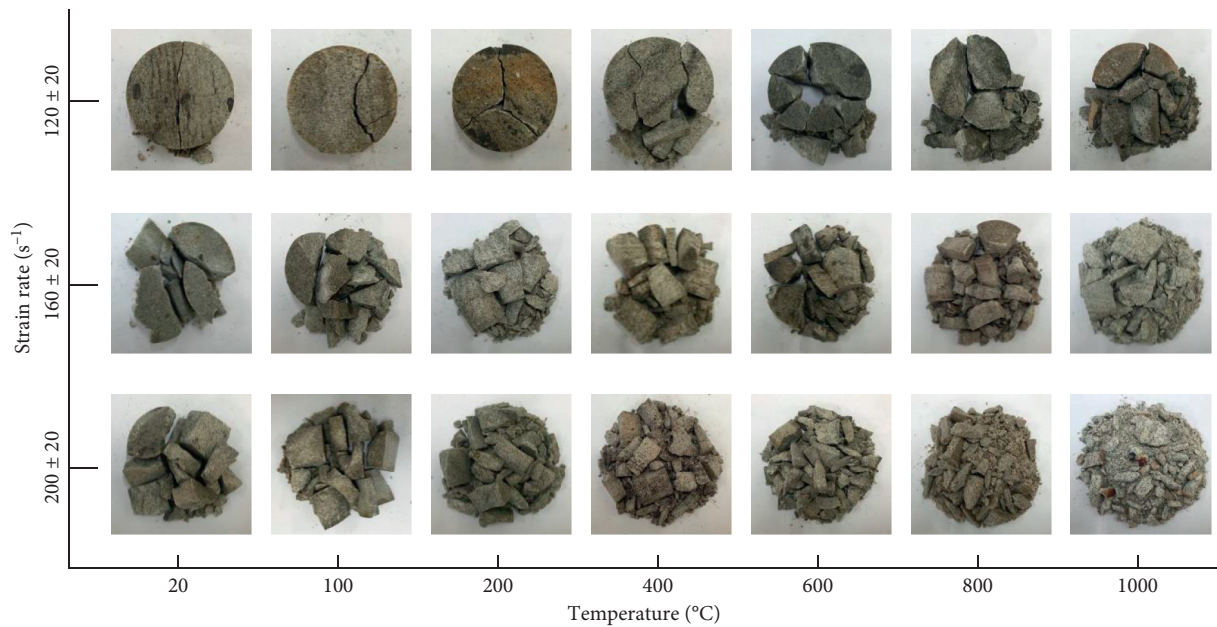


FIGURE 14: Dynamic failure mode of argillaceous sandstone after high temperature.

for specimen after 20°C, 100°C, 200°C, and 400°C, and specimen fractured into two or three pieces. With the increase of high temperature and strain rate, both the fracture surface and fragmentation degree of argillaceous sandstone specimen gradually increased.

3.6. SEM and EDS Results of Argillaceous Sandstone. Rock was a complex multiphase composite heterogeneous material, and the variation in microstructure could reflect the damage deterioration degree of argillaceous sandstone caused by high temperature, which further affected its mechanical behavior. The argillaceous sandstone samples for conducting SEM and EDS tests were soaked in alcohol for 5 min to remove the surface impurities and then dried for more than 12 h under 105°C. The prepared samples are shown in Figure 15.

Sedimentary rocks could be divided into five basic types: clastic structure, muddy structure, authigenic particle structure, biological skeleton structure, and crystalline structure [41, 42]. Figure 16 displays the microstructure

characteristics of argillaceous sandstone after different high temperatures obtained by SEM and EDS tests. From the electron microscopic scanning image (Figure 16(a)), it could be seen that the argillaceous sandstone was clastic structure and consisted of mineral particles with different sizes. Moreover, its interior was dense and only contained some tiny connection cracks at 20°C (room temperature), as shown in Figure 16(b). After 100~1000°C heat treatment, the granular crystals of the clastic structure gradually became larger; meanwhile, both the number and average size of the original pores decreased, and the initial cracks increased obviously, as shown in Figures 16(c)–16(n). After 20°C (room temperature), when the magnification was $\times 4000$, large numbers of fine and isolated cracks and pores could be observed inside argillaceous sandstone specimen. Above 800°C, the crystal gradually appeared tear ridge and became the main fracture form, and the crack appeared locally and gradually expanded; in addition, a large number of cracks and holes inside argillaceous sandstone connected with each other, which was one of the reasons for the weakening of mechanical properties of argillaceous sandstone.

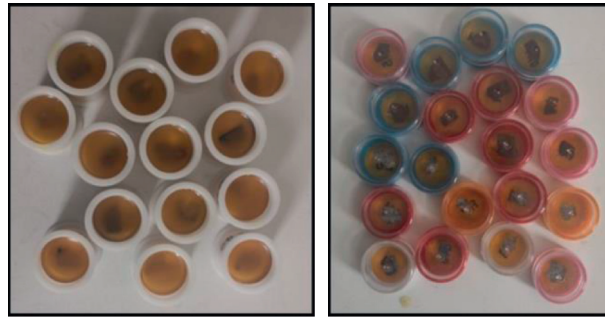


FIGURE 15: Prepared argillaceous sandstone samples for SEM and EDS tests.

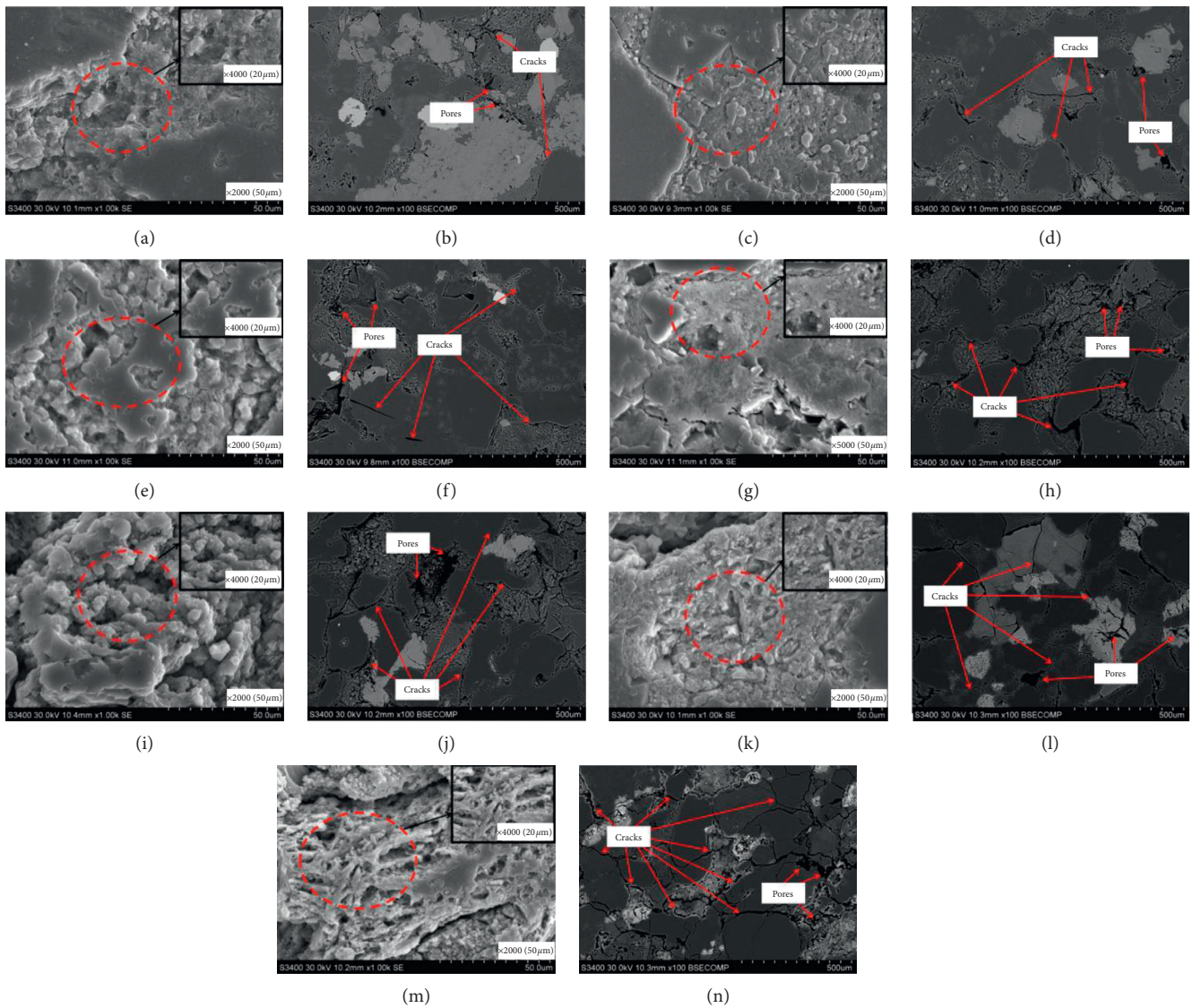


FIGURE 16: Microstructure characteristics of argillaceous sandstone after high temperatures treatment: (a) 20. (b) 20. (c) 100. (d) 100. (e) 200. (f) 200. (g) 400. (h) 400. (i) 600. (j) 600. (k) 800. (l) 800. (m) 1000. (n) 1000. (a, c, e, g, i, k, m) SEM results, enlarged $\times 2000$ and $\times 4000$; (b, d, f, h, j, l, n) EDS results.

4. Conclusions

- (1) With the increases of temperature, the peak stress gradually decreased and showed remarkable strain rate effect, while the peak strain gradually increased. The temperature response to the critical points of the peak strength was about 400°C. The incident energy gradually decreased with increasing temperature under air-dried and saturated states. The specific energy absorption values and the mass fractal dimensions showed positive correlation.
- (2) Under static load, shear and splitting failure modes were observed for argillaceous sandstone specimen after 20°C, 100°C, and 200°C. After 400°C, 600°C, and 800°C, the argillaceous sandstone specimen presented coupled shear and splitting failure. However, the collapse appeared after 1000°C under external load. Under dynamic load, tensile cracks were observed for specimen after 20°C, 100°C, 200°C, and 400°C, and specimen fractured into two or three pieces.
- (3) SEM and EDS test results indicated that, after 100~1000°C, the granular crystals of the clastic structure gradually became larger; meanwhile, both the number and average size of the original pores decreased, and the initial cracks increased obviously. Above 800°C, the crystal gradually appeared tear ridge to become the main form of fracture, and the crack appeared locally and gradually expanded.

Data Availability

The datasets generated and analyzed during the current study are available from the corresponding author upon reasonable request.

Conflicts of Interest

The authors declare that there are no conflicts of interest regarding the publication of this paper.

Acknowledgments

This work was financially supported by the Anhui Provincial Natural Science Foundation (no. 2008085QE220 and no. 1908085QE212), project funded by China Postdoctoral Science Foundation (no. 2019M652162), and Doctoral Fund Project of Anhui University of Science and Technology (no. 13190025 and no. 11695). Thanks are due to the State Key Laboratory of Mining Response and Disaster Prevention and Control in Deep Coal Mine for providing the experiment conditions.

References

- [1] Q. Qian, X. Zhou, and E. Xia, "Effects of the axial in situ stresses on the zonal disintegration phenomenon in the surrounding rock masses around a deep circular tunnel," *Journal of Mining Science*, vol. 48, no. 2, pp. 276–285, 2012.
- [2] X. Zhou, Q. Qian, and H. Song, "The effects of three-dimensional penny-shaped cracks on zonal disintegration of the surrounding rock masses around a deep circular tunnel," *Acta Mechanica Sinica*, vol. 28, no. 6, pp. 722–734, 2015.
- [3] S. Xie, H. Lin, Y. Chen, R. Yong, W. Xiong, and S. Du, "A damage constitutive model for shear behavior of joints based on determination of the yield point," *International Journal of Rock Mechanics and Mining Sciences*, vol. 128, Article ID 104269, 2020.
- [4] Y. L. Tan, X. S. Liu, B. Shen, Q. H. Gu, and J. G. Ning, "New approaches to testing and evaluating the rockburst risk of coal seam with hard roof and/or floor in coal mines," *Geomechanics and Engineering*, vol. 14, no. 4, pp. 367–376, 2018.
- [5] L. Chen, Q. W. Li, J. M. Yang, and Q. Li, "Laboratory testing on energy absorption of high-damping rubber in a new bolt for preventing rockburst in deep hard rock mass," *Shock and Vibration*, vol. 2018, Article ID 7214821, 12 pages, 2018.
- [6] Y. Shen, H. Yang, J. Xi, Y. Yang, Y. Wang, and X. Wei, "A novel shearing fracture morphology method to assess the influence of freeze-thaw actions on concrete-granite interface," *Cold Regions Science and Technology*, vol. 169, Article ID 102900, 2020.
- [7] L. Róg, "Vitrinite reflectance as a measure of the range of influence of the temperature of a georeactor on rock mass during underground coal gasification," *Fuel*, vol. 224, pp. 94–100, 2018.
- [8] W. Zhang, Q. Sun, Y. Zhu, and W. Guo, "Experimental study on response characteristics of micro-macroscopic performance of red sandstone after high-temperature treatment," *Journal of Thermal Analysis and Calorimetry*, vol. 136, no. 5, pp. 1935–1945, 2019.
- [9] J. Yu, G. Y. Liu, Y. Y. Cai, J. F. Zhou, S. Y. Liu, and B. X. Tu, "Time-dependent deformation mechanism for swelling soft-rock tunnels in coal mines and its mathematical deduction," *International Journal of Geomechanics*, vol. 20, no. 3, Article ID 04019186, 2020.
- [10] F.-Q. Gong, X.-F. Si, X.-B. Li, and S.-Y. Wang, "Dynamic triaxial compression tests on sandstone at high strain rates and low confining pressures with split hopkinson pressure bar," *International Journal of Rock Mechanics and Mining Sciences*, vol. 113, pp. 211–219, 2019.
- [11] H. B. Li, J. Zhao, J. R. Li, Y. Q. Liu, and Q. C. Zhou, "Experimental studies on the strength of different rock types under dynamic compression," *International Journal of Rock Mechanics and Mining Sciences*, vol. 41, no. 3, pp. 68–73, 2004.
- [12] R. Chen, K. Li, K. W. Xia, Y. L. Lin, W. Yao, and F. Y. Lu, "Dynamic fracture properties of rocks subjected to static pre-load using notched semi-circular bend method," *Rock Mechanics and Rock Engineering*, vol. 49, no. 10, pp. 3855–3864, 2016.
- [13] X. Li, Z. Zhou, T.-S. Lok, L. Hong, and T. Yin, "Innovative testing technique of rock subjected to coupled static and dynamic loads," *International Journal of Rock Mechanics and Mining Sciences*, vol. 45, no. 5, pp. 739–748, 2008.
- [14] W. Zhang, Q. Sun, S. Hao, and B. Wang, "Experimental study on the thermal damage characteristics of limestone and underlying mechanism," *Rock Mechanics and Rock Engineering*, vol. 49, no. 8, pp. 2999–3008, 2016.
- [15] T. Yin, Y. Wu, Q. Li, C. Wang, and B. Wu, "Determination of double-K fracture toughness parameters of thermally treated granite using notched semi-circular bending specimen," *Engineering Fracture Mechanics*, vol. 226, Article ID 106865, 2020.
- [16] J. Li, X. L. Guo, G. H. Liu, S. Q. Liu, and Y. Xi, "New analytical method to evaluate casing integrity during hydraulic

- fracturing of shale gas wells,” *Shock and Vibration*, vol. 2019, Article ID 4253241, 19 pages, 2019.
- [17] X. S. Liu, J. G. Ning, Y. L. Tan, and Q. H. Gu, “Coordinated supporting method of gob-side entry retaining in coal mines and a case study with hard roof,” *Geomechanics and Engineering*, vol. 15, no. 6, pp. 1173–1182, 2018.
- [18] W. Zhang, Q. Sun, S. Hao, J. Geng, and C. Lv, “Experimental study on the variation of physical and mechanical properties of rock after high temperature treatment,” *Applied Thermal Engineering*, vol. 98, pp. 1297–1304, 2016.
- [19] Q. Sun, W. Zhang, T. Su, and S. Zhu, “Variation of wave velocity and porosity of sandstone after high temperature heating,” *Acta Geophysica*, vol. 64, no. 3, pp. 633–648, 2016.
- [20] Y. Zhang, Q. Sun, and J. Geng, “Olivine thermal diffusivity influencing factors,” *Journal of Thermal Analysis and Calorimetry*, vol. 132, no. 1, pp. 7–16, 2018.
- [21] W. C. Zhu, J. Wei, L. L. Niu, S. Li, and S. H. Li, “Numerical simulation on damage and failure mechanism of rock under combined multiple strain rates,” *Shock and Vibration*, vol. 2018, Article ID 4534250, 20 pages, 2018.
- [22] S. B. Tang, C. Y. Yu, M. J. Heap, P. Z. Chen, and Y. G. Ren, “The influence of water saturation on the short- and long-term mechanical behavior of red sandstone,” *Rock Mechanics and Rock Engineering*, vol. 51, no. 9, pp. 2669–2687, 2018.
- [23] Q.-L. Ding, F. Ju, X.-B. Mao, D. Ma, B.-Y. Yu, and S.-B. Song, “Experimental investigation of the mechanical behavior in unloading conditions of sandstone after high-temperature treatment,” *Rock Mechanics and Rock Engineering*, vol. 49, no. 7, pp. 2641–2653, 2016.
- [24] Q.-B. Meng, C.-K. Wang, J.-F. Liu, M.-W. Zhang, M.-M. Lu, and Y. Wu, “Physical and micro-structural characteristics of limestone after high temperature exposure,” *Bulletin of Engineering Geology and the Environment*, vol. 79, no. 3, pp. 1259–1274, 2020.
- [25] S. Liu and J. Xu, “Study on dynamic characteristics of marble under impact loading and high temperature,” *International Journal of Rock Mechanics and Mining Sciences*, vol. 62, pp. 51–58, 2013.
- [26] S. Liu and J. Xu, “An experimental study on the physico-mechanical properties of two post-high-temperature rocks,” *Engineering Geology*, vol. 185, pp. 63–70, 2015.
- [27] T. B. Yin, K. Peng, L. Wang, P. Wang, X. Y. Yin, and Y. L. Zhang, “Study on impact damage and energy dissipation of coal rock exposed to high temperatures,” *Shock and Vibration*, vol. 2016, Article ID 5121932, 10 pages, 2016.
- [28] Y. Li, Y. Zhai, C. Wang, F. Meng, and M. Lu, “Mechanical properties of Beishan granite under complex dynamic loads after thermal treatment,” *Engineering Geology*, vol. 267, Article ID 105481, 2020.
- [29] S. Miao and Y. Zhou, “Temperature dependence of thermal diffusivity and conductivity for sandstone and carbonate rocks,” *Journal of Thermal Analysis and Calorimetry*, vol. 131, no. 2, pp. 1647–1652, 2018.
- [30] J. Geng, Q. Sun, Y. Zhang, L. Cao, C. Lü, and Y. Zhang, “Temperature dependence of the thermal diffusivity of sandstone,” *Journal of Petroleum Science and Engineering*, vol. 164, pp. 110–116, 2018.
- [31] T. Yin, Q. Li, and X. Li, “Experimental investigation on mode I fracture characteristics of granite after cyclic heating and cooling treatments,” *Engineering Fracture Mechanics*, vol. 222, Article ID 106740, 2019.
- [32] S. R. Wang, P. Hagan, Y. H. Zhao, X. Chang, K. I. Song, and Z. S. Zou, “The effect of confining pressure and water content on energy evolution characteristics of sandstone under stepwise loading and unloading,” *Advances in Civil Engineering*, vol. 2018, Article ID 4751612, 8 pages, 2018.
- [33] S. Tang, “The effects of water on the strength of black sandstone in a brittle regime,” *Engineering Geology*, vol. 239, pp. 167–178, 2018.
- [34] C. Yu, S. Tang, C. a. Tang et al., “The effect of water on the creep behavior of red sandstone,” *Engineering Geology*, vol. 253, pp. 64–74, 2019.
- [35] ISRM, *The Complete ISRM Suggested Methods for Rock Characterization, Testing and Monitoring*, R. Ulusay and J. Hudson, Eds., pp. 1974–2006, International Society for Rock Mechanics, Lisbon, Portugal, 2007.
- [36] F. Dai, Y. Xu, T. Zhao, N.-w. Xu, and Y. Liu, “Loading-rate-dependent progressive fracturing of cracked chevron-notched Brazilian disc specimens in split hopkinson pressure bar tests,” *International Journal of Rock Mechanics and Mining Sciences*, vol. 88, pp. 49–60, 2016.
- [37] X. Si, F. Gong, X. Li, S. Wang, and S. Luo, “Dynamic mohr-coulomb and hoek-brown strength criteria of sandstone at high strain rates,” *International Journal of Rock Mechanics and Mining Sciences*, vol. 115, pp. 48–59, 2019.
- [38] R. R. Zhang and L. W. Jing, “Analysis on the fragment and energy dissipation of deep sandstone after high/low temperature treatment in SHPB tests,” *Journal of China Coal Society*, vol. 43, no. 7, pp. 1884–1892, 2018.
- [39] Z. Zhou, X. Cai, D. Ma et al., “Water saturation effects on dynamic fracture behavior of sandstone,” *International Journal of Rock Mechanics and Mining Sciences*, vol. 114, pp. 46–61, 2019.
- [40] Q. Ma, D. Ma, and Z. Yao, “Influence of freeze-thaw cycles on dynamic compressive strength and energy distribution of soft rock specimen,” *Cold Regions Science and Technology*, vol. 153, pp. 10–17, 2018.
- [41] W.-L. Tian, S.-Q. Yang, Y.-H. Huang, and B. Hu, “Mechanical behavior of granite with different grain sizes after high-temperature treatment by particle flow simulation,” *Rock Mechanics and Rock Engineering*, vol. 53, no. 4, pp. 1791–1807, 2020.
- [42] D. Zheng and Q. Li, “An explanation for rate effect of concrete strength based on fracture toughness including free water viscosity,” *Engineering Fracture Mechanics*, vol. 71, no. 16–17, pp. 2319–2327, 2004.